THREE-DIMENSIONAL SIMULATIONS OF NATIONAL IGNITION FACILITY CAPSULE IMPLOSIONS WITH HYDRA

M. M. Marinak

S. W. Haan

R. E. Tipton

Introduction

Hydrodynamic instabilities are of critical importance in inertial confinement fusion (ICF) since they place fundamental limits on the design parameters required for capsule ignition. In capsule implosions in the National Ignition Facility (NIF), hydrodynamic instabilities are expected to evolve into the weakly nonlinear regime, so that nonlinear saturation of instability growth will control the amplitudes attained by perturbations in the shell. For perturbations with the same wave number, growth in the linear regime is the same in two and three dimensions. However, simulations of the Rayleigh–Taylor (RT) instability on classical interfaces[1–5]—as well as on foils driven by laser light[6,7] and x rays[8]—predict that symmetric three-dimensional (3-D) perturbations should grow largest in the nonlinear regime. An earlier potential flow model by Layzer[9] showed that round 3-D bubbles achieve the largest rise velocities. An increase in saturation amplitude with symmetry of the mode shape was seen in an extension of the potential flow model[10] and also with third-order perturbation theory.[11] Nova experiments done with planar foils driven by x rays exhibited this shape dependence, in quantitative agreement with simulations done with the HYDRA 3-D radiation hydrodynamics code. The larger, nonlinear saturation amplitudes attained by 3-D perturbations are a principal reason that simulations of surfaces with realistic 3-D perturbations are important to ICF research.

This article presents results from the first direct 3-D simulations of the NIF point-design (PT) capsule, which were performed with HYDRA. The effect of saturated hydrodynamic instability growth on NIF capsule implosions had been modeled previously using weakly nonlinear saturation analysis[12] and 2-D multimode simulations with LASNEX.[13–15] Direct 3-D numerical simulations most accurately treat saturation effects and multimode coupling for capsules with realistic surface perturbations in the presence of multiple shocks, ablation, convergence, and finite shell thickness.

In this article, we begin by describing the HYDRA radiation hydrodynamics code, which performed these simulations. Descriptions of the NIF PT capsule and of the scope of these simulations follow. Finally, we discuss results from a number of multimode simulations of hydrodynamic instabilities.

HYDRA

HYDRA is a 3-D radiation hydrodynamics code based upon a block structured mesh, which has Arbitrary Lagrange Eulerian (ALE) capability. An operator splitting technique is used to treat each of the physical processes in HYDRA separately and to combine the results. The Lagrangian phase solves the compressible hydrodynamic equations using a monotonic form of artificial viscosity,[16] with predictor-corrector time stepping. A control volume technique is used to calculate surface areas and volumes of the hexahedral elements. This technique results in a consistent set of surfaces and volumes on distorted meshes while conserving momentum. The ALE capability allows the mesh to be remapped according to a specified grid motion algorithm, using Van Leer advection in these simulations.[17] Material interfaces are maintained with an Eulerian interface tracker, which is based upon the volume fraction method,[18] generalized to run on arbitrary hexahedrons. "Mixed" zones, which contain one or more material interfaces, are subdivided into separate components for each material.

Radiation transport is treated in a multigroup diffusion routine using tabular opacities. A thermonuclear burn package was installed that treats fusion reactions, including the production and depletion of isotope concentrations, with reaction cross sections obtained from the Thermonuclear Data File (TDF) library.[19] Energetic charged particles are transported using an efficient multigroup algorithm.[20] It is an extension of diffusion, which retains the straight-line motion of particles undergoing collisions with electrons. Charged particles deposit momentum and energy into the fluid as they slow down, with the energy deposition divided among separate electron and ion channels. The user can specify independently the isotopes for which concentrations are to be followed and the energetic particle species which are to be transported. Since ICF capsules are thin to neutrons, an accurate treatment of neutron energy deposition is obtained with a model based upon an analytic solution to the neutron transport equations in the free-streaming limit. In the calculations presented here, the neutrons that interact with the capsule locally deposit the energy exchanged. Electron and ion conduction are treated, as well as electron–ion energy exchange, using coefficients from the model of Lee and More.[21]

By coupling several adjacent zones together, the user obtains greater freedom in zoning without the additional computational overhead and increased memory requirements associated with an unstructured mesh. Coupling the zones is essential to avoid the small Courant time step limits that would occur, for example, in narrow zones near the center or the pole of a mesh used in a 3-D capsule implosion simulation. This capability can be applied in the presence of mixed zones.

Several forms of the equations of state (EOS) are available, including the EOS4 tabular database and the inline quotidian EOS (QEOS). HYDRA runs on workstations and on vector supercomputers, and currently runs in parallel on the shared memory Cray J-90 SMP using multitasking.

Besides the planar foil simulations mentioned earlier,[5] HYDRA has been applied extensively to model Nova capsule implosions.[22]

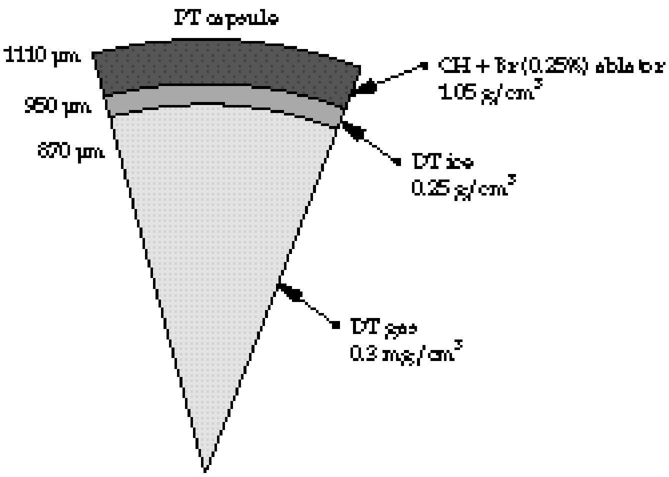

FIGURE 1. Schematic of the "point design" PT capsule shell. (50-05-0896-2031pb01)

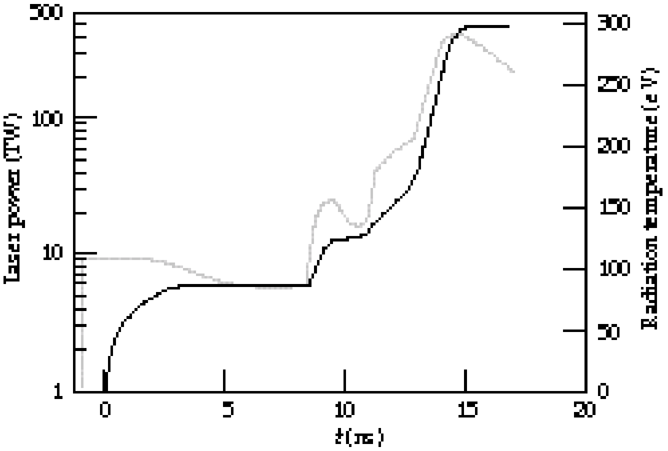

FIGURE 2. Laser power vs time to drive the PT target (gray curve, left scale), and temperature vs time optimal for the PT capsule (solid curve, right scale). (50-05-0896-2032pb01)

Point Design (PT) Capsule

The baseline capsule for the NIF, called the PT for "point design," has a 160-µm-thick polystyrene ablator doped with bromine (Fig. 1). The ablator encloses an 80-µm-thick layer of cryogenic DT ice. DT gas in equilibrium with the ice fills the capsule center at a density of 0.3 mg/cm^3. The capsule is mounted in a gold cylindrical hohlraum 9.5 to 10.0 mm long by 5.5 mm in diameter.

The laser pulse is staged in order to implode the capsule on a low-entropy adiabat (Fig. 2). This pulse delivers 1.35 MJ of laser light, 150 kJ of which is absorbed by the capsule. This 1.35-MJ pulse, which is somewhat less than NIF's maximum (1.8 MJ), was chosen to leave an extra margin for errors in modeling. The light comes into each laser entrance hole in two cones. The relative power in these cones is dynamically varied to minimize the time-varying pole-to-waist asymmetry, which is described as a P_2 Legendre polynomial. Since the NIF has 192 beams clustered in groups of four, there are effectively eight spots in each of the inner cones and 16 in the outer cones. In the absence of significant pointing and power balance errors, the intrinsic azimuthal variation in the hohlraum flux is small. With the standard cylindrical hohlraum, the drive asymmetries are designed to be nearly 2-D. The capsule surface roughness should be the primary source of 3-D asymmetries in the implosion.

The capsule-only simulations presented here model the hydrodynamic instabilities seeded by surface roughness. The average hohlraum flux obtained from an integrated LASNEX simulation[3] is imposed on the capsule. Hydrodynamic instabilities are simulated over a portion of the capsule solid angle, which extends equal amounts in the polar and azimuthal angles ($\Delta\theta$, $\Delta\varphi$), with one of the boundaries coincident with the capsule equator. Multimode perturbations imposed are of the form $G(\theta, \varphi) = \sum_m \sum_n a_{mn} \cos\left(\frac{m\pi\theta}{\Delta\theta}\right)\cos\left(\frac{n\pi\varphi}{\Delta\varphi}\right)$ where a_{mn}

is the mode coefficient. Symmetry conditions exist at the transverse boundaries. These modes are the 3-D analog to the modes used in 2-D axisymmetric simulations performed over a portion of a quadrant.

Perturbations initialized on the outer ablator surface are based on traces from Nova capsules, while those on the inner DT surface are based on measurements of cryogenic ice. The data are Fourier analyzed to obtain a 1-D power spectrum. This spectrum may be shifted in mode number when applying the information to the PT capsule, which has a larger radius. The 1-D spectrum is converted to an estimated 3-D power spectrum[23] and the power is distributed isotropically among the 3-D modes with equivalent wave number. Equivalent mode amplitudes from the spectra used in the simulations are shown in Fig. 3 as a function of the l mode number. Random phase factors are assigned to a_{mn} so that the topology of the surface does not have unusually large peaks and valleys due to excessive phase coherence.

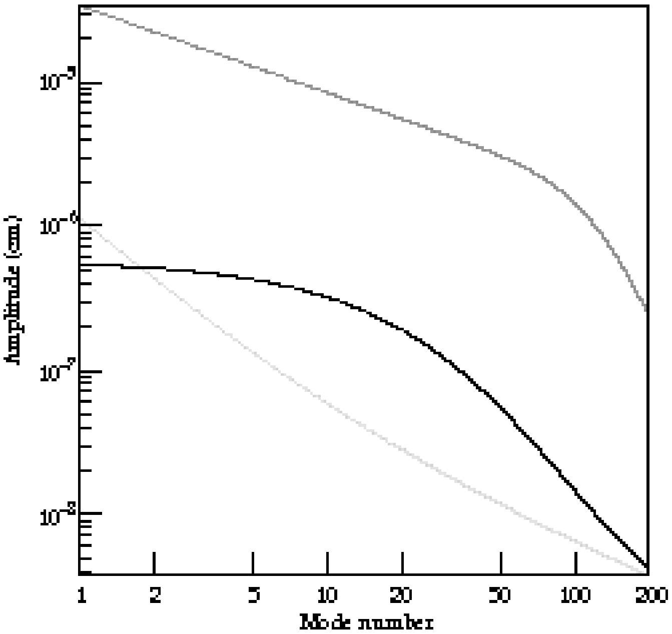

FIGURE 3. Surface perturbation spectra used in simulations of NIF PT capsules. The black curve is the early spectrum for the ablator surface obtained from measurements of a Nova capsule. The light gray curve is the spectrum from a more recent measurement of an optimized Nova capsule. The dark gray curve shows the spectrum of the ice surface. (50-05-0996-2212pb01)

Multimode Simulation Results

We consider first a capsule with perturbation amplitudes, in the range of modes $l = 10$–1000, equal to 24 nm rms on the outer surface and 1 μm rms on the inner cryogenic DT surface. A domain extending 18° in each angle is used to simulate modes in the range $l = 10$–40. The grid used here measured 32 × 32 × 169 zones in the polar, azimuthal, and radial directions respectively, so that there are at least 16 transverse zones per wavelength for the least well resolved modes. As the laser pulse rises to peak power, it generates four staged shocks that compress the capsule shell, reducing the shell thickness to 20 μm early in the implosion phase. The grid motion algorithm employed follows this large change in shell aspect ratio and ensures that perturbation growth in the shell is resolved by zones with a fine spacing of 0.75 μm in the radial direction.

Perturbations that grow on the simulated ablator are seeded by initial ablator surface roughness and by the perturbed rarefaction wave that returns from the inner ice surface after the first inward-going shock arrives. During the implosion phase, the shell areal density $A(\theta,\varphi) = \int \rho(r,\theta,\varphi)\, dr$ strongly resembles the initial outer surface perturbation, indicating that modes growing in the ablator are seeded predominantly by ablator surface perturbations. Valleys initially on the ablator surface develop into bubbles on the ablator, surrounded by interconnecting spike sheets and larger individual spikes, as shown by the iso-density contour plot Fig. 4(a).

Figure 4(b) shows bubble and spike ridge structures that are growing on the pusher–hot spot interface after

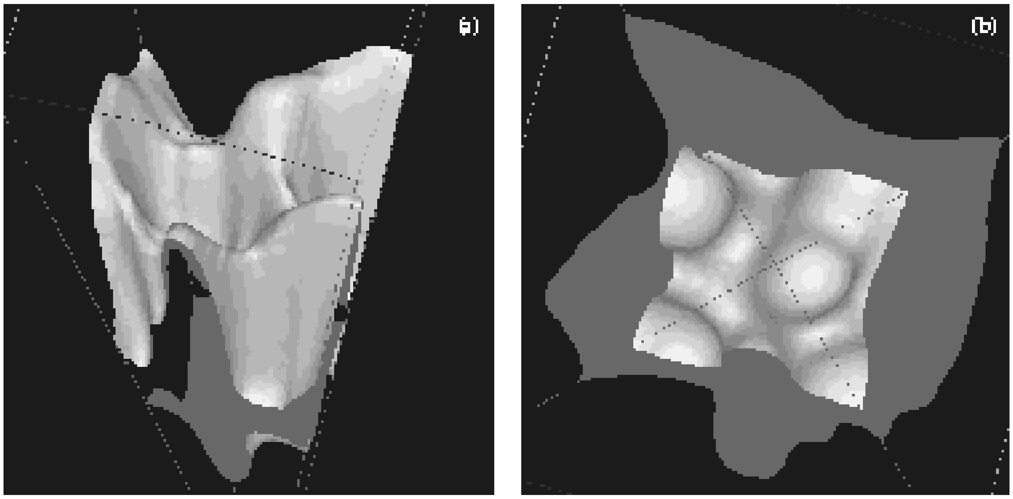

FIGURE 4. Two perspectives of the iso-density contours of 60 g/cm^3 at 17.0 ns from a PT capsule simulation having 24-nm– and 1-μm–rms perturbations initially on the outer ablator and inner ice surfaces, respectively. Multimode perturbations with $l = 10$–40 were initialized. (a) View of region just inside of the DT–ablator interface. (b) View of pusher–hot spot interface. (50-05-0896-2033pb01)

the rebounding shock has reached it. The locations of these bubbles correspond to the locations of equivalent structures in the ablator, which have fed through the shell. The resemblance to the imposed surface perturbation is characteristic of weakly nonlinear behavior. Some degree of roll-up is apparent, due to a Kelvin Helmholtz instability,[7,9,10] but it is much less than was observed on the classical fuel–pusher interface in Nova capsule simulations.[20,22] The structure of these perturbations has much power in modes $l \lesssim 40$. These growing structures remain visible until the capsule reaches peak compression and the hot spot achieves ignition conditions, with a column density of $\rho r \sim 0.3$ g/cm^3 and ion temperature of ~10 keV. As the capsule reaches peak compression and begins to ignite, the inner surface structure evolves toward lower mode numbers characterized by $l = 10$–15. This behavior appears to be strongly influenced by ablation driven by conduction from the hot spot and the effect of convergence, rather than by mode coupling, as was seen in planar geometry.[7,24–27] Since the shell has a peak convergence ratio of 37, there is a large decrease in the wavelength associated with a particular mode number during the implosion. At ignition the deposition of alpha particles is mostly responsible for "bootstrapping" the central temperature to over 60 keV. This burn propagates into the fuel layer, which has a peak density of > 1000 g/cm^3 at this time. Simulations are carried into the expansion phase for as long as the capsule continues to burn at a significant rate.

Figure 5 shows yields from simulations of several PT capsules that have different multimode surface perturbations with modes $l = 10$–40. The capsule with the largest perturbation amplitudes failed to ignite because, at the time of stagnation, spikes had penetrated 10 µm into the 30-µm-radius hot spot, and bubbles were burning through the shell. Quench of ignition in the DT capsule by 10-µm spikes is consistent with results obtained with other modeling techniques.[3] The location of the yield cliff in Fig. 5 corresponds to a roughness on the outer surface which is ~40% smaller than that obtained with 2-D multimode simulations over this range of modes.[3,4] Higher nonlinear saturation amplitudes and nonlinear growth rates occur for the round, 3-D-bubble-spike features than for the 2-D bubble ridges, and these are responsible for the smaller allowable surface roughness. Differences in instability growth are illustrated by comparing results from one of these 3-D multimode simulations with an axisymmetric 2-D HYDRA simulation that also has surface perturbations consisting of modes $l = 10$–40. The initial rms value for roughness on the capsule surfaces is identical for these 2-D and 3-D simulations. The roughnesses correspond to surfaces with overall perturbations of 19.4 nm and 1.0 µm rms on the ablator and ice surfaces respectively. These amplitudes were chosen so that perturbations would evolve into the weakly nonlinear regime. Figure 6 compares filled contour plots of density on the domain boundaries at 17.0 ns for the 2-D and 3-D simulations with equivalent surface roughnesses. The larger saturated amplitudes attained by the 3-D perturbations are clearly apparent. Since the larger 3-D ablator bubbles are close to penetrating the shell, the bubble tips accelerate,[22] thereby increasing the apparent difference between the growth of 2-D and 3-D bubbles.

The nonlinear growth of the 3-D multimode perturbations is affected by mode coupling and perturbation shape effects. Broad bubbles and narrow

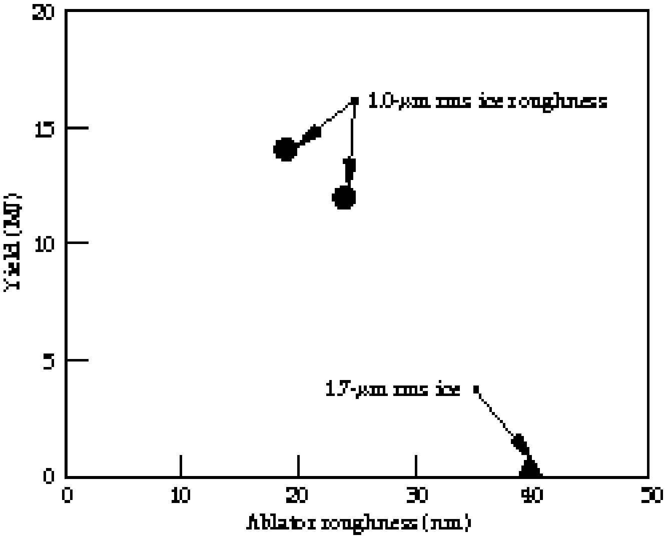

FIGURE 5. Yields for several PT capsule simulations having multimode perturbations with $l = 10$–40 at both the ablator and inner DT-ice surfaces. Ice surface roughness was varied while the ablator roughness was fixed at 24 nm. (50-05-0896-2034pb01)

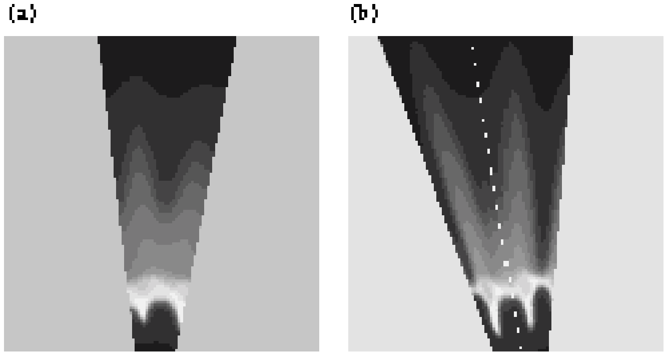

FIGURE 6. Filled contour plots of density at 17.0 ns for two capsules each having initial roughnesses equivalent to 19 nm rms and 1.0 µm rms on the ablator and DT-ice surfaces, respectively. Contours are shown along the planar boundaries of the domains simulated with the radial direction extending upward. Both perturbations contain modes with $l = 10$–40. Perturbation in (a) is 2-D axisymmetric while perturbation in (b) is 3-D, shown along two orthogonal boundary planes. The lightest color corresponds to peak density. (50-05-0896-2035pb01)

spike sheets begin to form early in the nonlinear regime, and for a time it can be described by second-order mode coupling theory.[24,28] Nearby structures strongly influence the evolution of individual bubbles and spikes in the nonlinear phase. Previous attempts to estimate the effect of the higher 3-D saturation amplitudes within direct 2-D axisymmetric capsule simulations involved placing a single bubble or spike on the pole. This treatment is limited because it cannot reproduce the complex multimode coupling and interference effects that occur on a realistic 3-D surface.

The simulations we have discussed so far contain initial perturbations with modes $l = 10–40$. Modes $40 < l < 120$, which are also RT unstable on the ablator, are much less capable of feeding through the shell and producing spikes during deceleration. The shorter length scales of their mode structures reduce their ability to feed through. But the shorter-wavelength modes can threaten the shell integrity during implosion, when the shell is thinnest. We now consider a simulation that includes modes spanning both of these ranges. Perturbations with modes $l = 15–120$ were simulated on both the inner ice and outer ablator surfaces on a 12° wedge. The grid measured 64 × 64 × 169 zones in the polar, azimuthal, and radial directions respectively. The outer surface perturbation corresponded to the best surface finish measured on a Nova capsule. Similar traces from Russian capsule shells, which have larger radii than Nova capsules, suggest that the long-wavelength surface roughness will not scale strongly to our disadvantage as we go to larger capsules.[29] Figure 7 shows contour plots of the initial perturbations simulated, which have amplitudes of 21 nm and 1.3 μm peak-to-valley on the outer ablator and inner DT ice surfaces, respectively.

Late in the implosion phase, the structure of the growing multimode perturbation has its peak amplitude at the classical interface between the polystyrene ablator and the DT fuel. Centered at this location, the perturbation will penetrate the shell when the amplitude is only a fraction of the shell thickness. The higher modes, which grow fastest on the classical ablator–DT interface, are of concern for the period before the peak implosion velocity is reached. After the implosion velocity peaks, convergence causes the capsule shell to thicken and the classical interface becomes RT stable. Although these perturbations continue to grow inertially, the rapid thickening of the shell separates the classical interface from the shell's inner surface fast enough that further growth of short wavelength modes is unimportant. The longer wavelength modes that feed through the shell, combined with perturbations on the inner capsule surface, assume principal importance once the rebounding shock begins to traverse the shell.

In the present simulation, the shell integrity was never threatened. Figure 8 shows the iso-density contours at 17.1 ns, when the capsule is close to igniting. The contour surface shown in Fig. 8(a) is located in the DT-fuel region of the shell, somewhat inside the polystyrene–DT interface, while the contour surface in Fig. 8(b) corresponds to the pusher–hot spot interface. The high modes apparent near the classical interface, typically near $l = 90$, have not fed through appreciably to the inner interface, which has features typically in the range $l = 15–20$. The yield (15.5 MJ) approaches that for an unperturbed capsule. Thus a PT capsule, with a surface finish equal to the best measured on a Nova capsule, easily ignites in the simulation. The margin of ignition in this simulation implies that substantially larger perturbation amplitudes can be tolerated on the outer surface, even with high-l modes present.

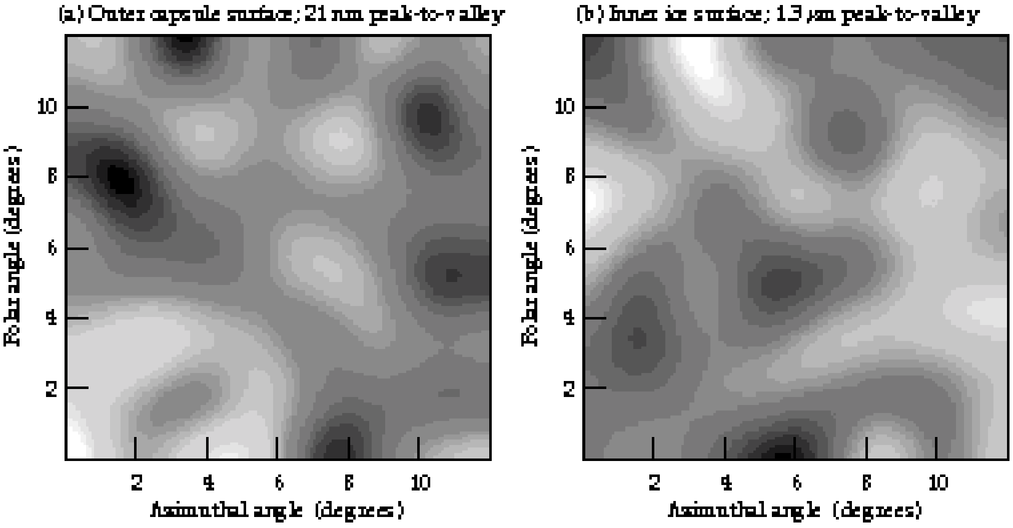

FIGURE 7. Contour plots of multimode perturbations initialized in simulation containing modes $l = 15–120$. (a) Ablator surface perturbation with peak-to-valley amplitude 21 nm. (b) Inner ice surface perturbation with peak-to-valley amplitude 1.3 μm. (50-05-0896-2036pb01)

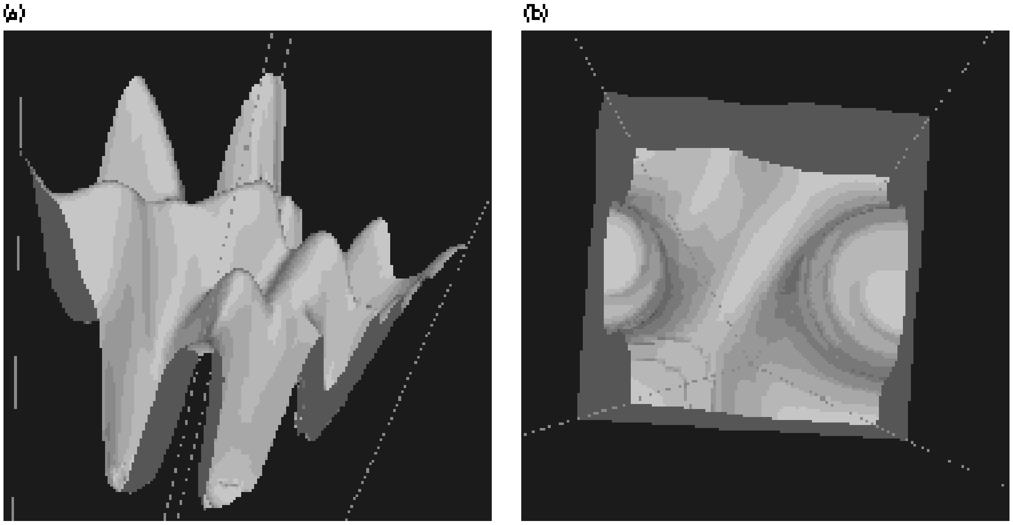

FIGURE 8. Iso-density contour surfaces near ignition time for a PT capsule simulation containing modes $l = 15–120$. (a) 130 g/cm^3 surface just inside the DT–ablator interface. (b) 650 g/cm^3 surface at pusher–hot spot interface. (50-05-0896-2037pb01)

Conclusions

We presented results from the first 3-D simulations of the NIF PT capsule design. Realistic multimode perturbations seeded hydrodynamic instabilities that evolved into the weakly nonlinear regime. These perturbations were characterized by broad round bubbles surrounded by interconnecting spike sheets and larger individual spikes. Simulations showed that modes with $l < 40$ could threaten ignition by feeding through the shell and developing into spikes when the shell decelerates. Higher modes are much less capable of generating spikes that quench ignition, but they can threaten shell integrity during the implosion phase. The simulations showed that the PT capsule can tolerate spikes with amplitudes up to 10 μm before ignition is quenched.

Three-dimensional multimode perturbations attained larger nonlinear amplitudes than 2-D multimode perturbations having the same initial rms roughness. This results in a constraint on the roughness of the ablator surface that is ~40% smaller than was obtained from 2-D multimode simulations over a similar range of modes. Even when modes spanning the range $l = 15–120$ were included, however, a PT capsule with surface finishes equal to the best currently attainable easily ignited in the simulation. Future simulations of the PT will quantify the sensitivity of the capsule to surface roughnesses contained in different ranges of modes.

Notes and References

1. G. Tryggvason and S. O. Unverdi, *Phys. Fluids A* **2** (5), 656–659 (1990).
2. T. Yabe, H. Hoshino, and T. Tsuchiya, *Phys. Rev. A* **44** (4), 2756–2758 (1991).
3. J. Hecht, D. Ofer, U. Alon, D. Shvarts, S. A. Orszag, and R. L. McCrory, *Laser Part. Beams* **13** (3), 423–440 (1995); D. Ofer, J. Hecht, D. Shvarts, Z. Zinamon, S. A. Orszag, and R. L. McCrory, *Proceedings of the 4th International Workshop on the Physics of Compressible Turbulent Mixing,* edited by P. F. Linden, D. L. Youngs, and S. B. Dalziel (Cambridge University Press, Cambridge, 1993), pp. 119–128.
4. H. Sakagami and K. Nishihara, *Phys. Rev. Lett.* **65** (4), 432–435 (1990).
5. R. P. J. Town and A. R. Bell, *Phys. Rev. Lett.* **67** (14), 1863–1866 (1991).
6. J. P. Dahlburg, J. H. Gardner, G. D. Doolen, and S. W. Haan, *Phys. Fluids B* **5** (2), 571–584 (1993).
7. J. P. Dahlburg, D. E. Fyfe, J. H. Gardner, S. W. Haan, S. E. Bodner, and G. D. Doolen, *Phys. Plasmas* **2** (6) 2453–2459 (1995).
8. M. M. Marinak, B. A. Remington, S. V. Weber, R. E. Tipton, S. W. Haan, K. S. Budil, O. L. Landen, J. D. Kilkenny, and R. Wallace, *Phys. Rev. Lett.* **75** (20), 3677–3680 (1995).
9. D. Layzer, *Astrophys. J.* **122** (1), 1–12 (1955).
10. J. Hecht, U. Alon, D. Shvarts, *Phys. Fluids* **6** (12), 4019–30 (1994).
11. J. W. Jacobs and I Catton, *J. Fluid Mech.* **187**, 329–352 (1988).
12. S. W. Haan, *Phys. Rev. A* **39** (11), 5812–5825 (1989).
13. G. B. Zimmerman and R. M. More, *J. Quant. Spectrosc. Radiat. Transfer* **23** (5), 517–522 (1980); R. M. More, *ibid*. **27** (3), 345–357 (1982).
14. S. W. Haan, S. M. Pollaine, J. D. Lindl, J. J. Suter, et al., *Phys. Plasmas* **2** (6), 2480–2487 (1995).

15. W. J. Krauser, N. M. Hoffman, D. C. Wilson, B. H. Wilde, W. S. Varnum, D. B. Harris, F. J. Swenson, P. A. Bradley, S. W. Haan, S. M. Pollaine, A. S. Wan, J. C. Moreno, and P. A. Amendt, *Phys. Plasmas* **3** (5), 2084–2093 (1996).
16. D. J. Benson, *Comp. Methods Appl. Mech. Eng.* **93**, 39–95 (1991).
17. B. Van Leer, *J. Comput. Phys.* **23** (3), 276–299 (1977).
18. D. L. Youngs, in *Numerical Methods for Fluid Dynamics,* edited by K. W. Morton and M. J. Baines (Academic Press, New York, 1982) pp. 273–285.
19. R. M. White, D. A. Resler, and S. I. Warshaw, in *Proceedings of the International Conference on Nuclear Data for Science and Technology,* 13–17 May 1991, *Jülich,* edited by S. M. Qaim (Springer–Verlag, Berlin, 1992) p. 834.
20. G. Zimmerman, private communication.
21. Y. T. Lee and R. M. More, *Phys. Fluids* **27** (5), 1273–1286 (1984).
22. M. M. Marinak, R. E. Tipton, O. L. Landen, T. J. Murphy, P. Amendt, S. W. Haan, S. P. Hatchett, C. J. Keane, R. McEachern, and R. Wallace, *Phys. Plasmas* **3** (65), 2070–2076 (1996).
23. S. M. Pollaine, S. P. Hatchett, and S. H. Langer, *ICF Quarterly Report*, **4** (3), 87–89, Lawrence Livermore National Laboratory, Livermore, CA, UCRL LR105821-94-3 (1994).
24. M. M. Marinak, R. E. Tipton, B. A. Remington, S. W. Haan, S. V. Weber, *ICF Quarterly Report,* **5** (3), 168–178, Lawrence Livermore National Laboratory, Livermore, CA, UCRL LR105821-95-3 (1995).
25. D. H. Sharp, *Physica D* **12** (1–3), 3–18 (1984).
26. U. Alon, D. Shvarts, and D. Mukamel, *Phys. Rev. E* **48** (2), 1008–1014 (1993); *Phys. Rev. Lett.* **72** (18), 2867–2870 (1994).
27. D. Shvarts, U. Alon, D. Ofer, R. L. McCrory, and C. P. Verdon, *Phys. Plasmas* **2** (6), 2465–2472 (1995).
28. S. W. Haan, *Phys. Fluids B* **3** (8), 2349–2355 (1991).
29. R. Cook, private communication.